

Higher harmonic generation by massive carriers in buckled two-dimensional hexagonal nanostructures

H. K. Avetissian and G. F. Mkrtchian*

Center of Strong Fields Physics, Yerevan State University, 1 A. Manukian, Yerevan 0025, Armenia



(Received 30 November 2018; revised manuscript received 31 January 2019; published 20 February 2019)

Generation of high harmonics in novel two-dimensional (2D) nanostructures such as silicene, germanene, and stanene initiated by strong coherent electromagnetic radiation of arbitrary polarization, taking into account the spin-orbit coupling and the buckling of two Bravais lattices, is investigated. The buckled hexagonal lattice system is described by the four-band second-nearest-neighbor tight-binding model. The developed theory of the interaction of massive (nonzero effective mass) carriers with a strong driving wave field covers the full Brillouin zone of a 2D hexagonal nanostructure. The wave-matter interaction is taken in the length gauge that provides proper inclusion of inter- and intraband transitions with nonzero Berry curvatures. The closed set of differential equations for the single-particle density matrix of massive carriers is solved numerically. The obtained results show that novel 2D nanostructures can serve as an effective medium for the generation of even and odd high harmonics of arbitrary polarization. Moreover, for the nanostructures under consideration, the role of the band topology is significant at harmonic generation.

DOI: [10.1103/PhysRevB.99.085432](https://doi.org/10.1103/PhysRevB.99.085432)

I. INTRODUCTION

The synthesis of graphene [1,2] stimulated the search for new nanomaterials with similar properties. The successes of the last decade in the field of nanotechnology have allowed synthesizing graphenelike nanostructures with a very high carrier mobility and, consequently, with a very small scattering of electrons. Among such nanostructures are silicene [3–5], germanene [6,7], and stanene [8]. These nanostructures, being synthesized after graphene, are exceptional examples of graphenelike nanostructures and have rich physics [9–16]. In particular, they consist of honeycomb lattices of atoms with buckled sublattices made of A and B sites. The low-energy dynamics in the K_+ and K_- valleys is described by the Dirac theory as in graphene. However, in these nanostructures, Dirac electrons are massive (have nonzero effective mass) compared to graphene ones due to a relatively large spin-orbit coupling (~ 65 meV in stanene) [10]. It is notable that the quasiparticles' mass can be controlled by applying the electric field perpendicular to the nanostructures sheet [9]. Wherein the topology of the bands is modified. In particular, the bands acquire Berry curvature [17]. These properties suggest that in these nanostructures one can expect novel nonlinear optical effects which are absent in graphene.

Recently, there has been growing interest in extending high harmonic generation (HHG) and related processes to bulk crystals [18–24] and two-dimensional (2D) nanostructures, such as graphene [25–38], hexagonal boron nitride [39], and monolayer transition-metal dichalcogenides [40]. There are several experiments that validated the main theoretical predictions. In particular, HHG in the XUV domain was generated in bulk crystals [18,19]. Note that the experiment [37] with

the generation of the ninth harmonic in graphene and the generation of harmonics extending to the 13th order in the 2D semiconductor [40] opened new avenue towards high harmonic generation in 2D nanostructures. HHG in atoms [41] is well described within a semiclassical three-step model including ionization, acceleration, and recollision of electrons with the original nucleus. The physics of HHG in solids is more complicated, and its description requires a comprehensive quantum-kinetic modeling of carriers' interband and intraband dynamics. The relative contribution of interband and intraband dynamics in the HHG process depends on the bands' structure and pump wave-pulse parameters. From this point of view, silicene, germanene, and stanene are of interest due to their rich physics of bands [10]. Up to now, to our knowledge, there has been no study of the HHG process in these materials. Hence, it is of actual interest to study the mentioned graphenelike nanostructures physics in the presence of intense optical fields that can lead to the effective generation of harmonics. Our interest is also motivated by the fact that these nanostructures have nontrivial topology of bands, which can be controlled by the electromagnetic fields [9–16].

In the present work, we develop a microscopic theory of a buckled 2D hexagonal lattice nonlinear interaction with strong electromagnetic radiation of arbitrary polarization beyond the Dirac cone approximation and applicable to the full Brillouin zone. The buckled hexagonal lattice system is described by the four-band second-nearest-neighbor tight-binding model, taking into account spin-orbit coupling. We solve quantum-kinetic equations for massive carriers. The light-matter interaction is taken in the length gauge that provides proper inclusion of inter- and intraband transitions with nonzero Berry curvatures. We investigate the generation of even and odd high harmonics of arbitrary polarization in these nanostructures by a midinfrared pump wave. We also consider the role of the

*mkrтчian@ysu.am

topology of bands in the nonlinear optical response of buckled hexagonal lattice.

This paper is organized as follows. In Sec. II the Hamiltonian within the tight-binding approximation is presented, and the set of equations for a single-particle density matrix is formulated. In Sec. III, we consider the high harmonic generation process. Finally, conclusions are given in Sec. IV.

II. EVOLUTIONARY EQUATION FOR THE SINGLE-PARTICLE DENSITY MATRIX

Along with graphene all considered nanostructures consist of a honeycomb lattice. However, in contrast to graphene these periodic honeycomb lattice structures become unstable in a planar structure. They stabilize at the nonzero buckling of two Bravais lattices; that is, every alternate atom in the nanostructure is buckled in the direction perpendicular to the lattice plane. The buckled hexagonal lattice with the chosen geometry is shown in Fig. 1. The vectors which connect nearest-neighbor atoms are

$$\begin{aligned} \delta_1 &= \left(\frac{a}{\sqrt{3}}, 0, -\ell \right), & \delta_2 &= \left(-\frac{a}{2\sqrt{3}}, \frac{a}{2}, -\ell \right), \\ \delta_3 &= \left(-\frac{a}{2\sqrt{3}}, -\frac{a}{2}, -\ell \right). \end{aligned} \quad (1)$$

The Bravais lattice is spanned by the basis vectors

$$\mathbf{a}_1 = \left(\frac{\sqrt{3}a}{2}, \frac{a}{2}, 0 \right), \quad \mathbf{a}_2 = \left(\frac{\sqrt{3}a}{2}, -\frac{a}{2}, 0 \right). \quad (2)$$

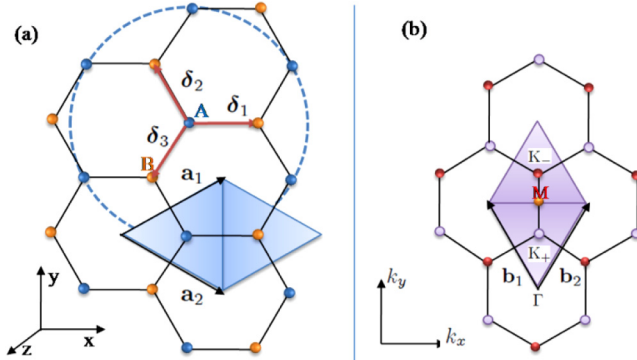


FIG. 1. (a) Buckled hexagonal lattice: The atoms labeled A are all in the xy plane ($z_A = 0$), and all the B atoms are located behind the plane at $z_B = -\ell$. Hence, the sheet is composed of two atomic planes: one of A atoms and another of B atoms. The vectors δ_1 , δ_2 , and δ_3 connect nearest-neighbor atoms. The dashed circle shows second-nearest-neighbor atoms of the same type. The vectors $\mathbf{a}_1 = \delta_1 - \delta_3$ and $\mathbf{a}_2 = \delta_1 - \delta_2$ are the two-dimensional basis vectors, and the shaded area is the unit cell with two atoms. (b) Reciprocal lattice of the triangular lattice. Its basis vectors are \mathbf{b}_1 and \mathbf{b}_2 . The reciprocal lattice unit cell is shown as a shaded rhombic area, with inequivalent K_+ and K_- points. The Γ point of the Brillouin zone and the M point are also shown.

The vectors which connect second-nearest-neighbor atoms are

$$\begin{aligned} \delta_1^{(2)} &= (0, a, 0), & \delta_2^{(2)} &= -\delta_1^{(2)}, & \delta_3^{(2)} &= \left(\frac{\sqrt{3}a}{2}, -\frac{a}{2}, 0 \right), \\ \delta_4^{(2)} &= -\delta_3^{(2)}, & \delta_5^{(2)} &= \left(\frac{\sqrt{3}a}{2}, \frac{a}{2}, 0 \right), & \delta_6^{(2)} &= -\delta_5^{(2)}. \end{aligned} \quad (3)$$

The reciprocal lattice unit cell is a rhombus formed by two vectors:

$$\mathbf{b}_1 = \left(-\frac{2\pi}{a\sqrt{3}}, \frac{2\pi}{a}, \right), \quad \mathbf{b}_2 = \left(\frac{2\pi}{a\sqrt{3}}, \frac{2\pi}{a}, \right). \quad (4)$$

The modules of the basis vectors yield the lattice spacings: a and $k_b = 4\pi/\sqrt{3}a$ in conventional and reciprocal space, respectively. The important crystallographic points, which are crucial for electronic properties of the nanostructure, are also shown. High-energy excitations are situated in the vicinity of the Γ point. Low-energy excitations are centered around the two points K_+ and K_- , represented by the vectors

$$\mathbf{K}_+ = \frac{k_b}{\sqrt{3}}\hat{\mathbf{y}}, \quad \mathbf{K}_- = \frac{2k_b}{\sqrt{3}}\hat{\mathbf{y}}. \quad (5)$$

Finally, the M point ($\mathbf{M} = \sqrt{3}k_b\hat{\mathbf{y}}/2$) is shown. The buckled hexagonal lattice system will be described by the four-band second-nearest-neighbor tight-binding model [10],

$$\begin{aligned} H &= -\gamma_0 \sum_{\langle i,j \rangle \alpha} c_{i\alpha}^\dagger c_{j\alpha} + i \frac{\lambda_{\text{SO}}}{3\sqrt{3}} \sum_{\langle\langle i,j \rangle\rangle \alpha\beta} v_{ij} c_{i\alpha}^\dagger \sigma_{\alpha\beta}^z c_{j\beta} \\ &\quad - \frac{\ell}{2} \sum_{i\alpha} \mu_i E_z c_{i\alpha}^\dagger c_{i\alpha}, \end{aligned} \quad (6)$$

where $c_{i\alpha}^\dagger$ creates an electron with spin polarization α at site i and $\langle i, j \rangle$ and $\langle\langle i, j \rangle\rangle$ run over all the nearest- and second-nearest-neighbor hopping sites, respectively. The first term in Eq. (6) represents the usual nearest-neighbor hopping with the transfer energy γ_0 . The second term [42] represents the effective spin-orbit coupling, where $\sigma = (\sigma_x, \sigma_y, \sigma_z)$ is the Pauli matrix of the spin, with $v_{ij} = +1$ if the next-nearest-neighbor hopping is counterclockwise and $v_{ij} = -1$ if it is clockwise with respect to the positive z axis. In order to control the mass term we assume the electric field E_z applied perpendicular to the nanostructure sheet which generates a staggered sublattice potential $\propto \ell E_z$ between atoms at A sites and B sites. Here $\mu_i = \pm 1$ for the A and B sites, respectively. Note that the first and second Rashba spin-orbit couplings are neglected because they are small compared with the spin-orbit coupling λ_{SO} between next-nearest-neighbor atoms.

By performing Fourier transformations and choosing the basis $\{|A\rangle, |B\rangle\} \otimes \{|\uparrow\rangle, |\downarrow\rangle\}$, from Eq. (6) we obtain the Hamiltonian

$$\hat{H} = \begin{bmatrix} \frac{1}{2}\sigma_z g(\mathbf{k}) - \frac{\ell}{2}E_z & -\gamma_0 f(\mathbf{k}) \\ -\gamma_0 f^*(\mathbf{k}) & -\frac{1}{2}\sigma_z g(\mathbf{k}) + \frac{\ell}{2}E_z \end{bmatrix}, \quad (7)$$

where

$$g(\mathbf{k}) = \frac{4}{3\sqrt{3}}\lambda_{\text{SOC}} \left[2 \cos\left(\frac{\sqrt{3}}{2}ak_x\right) \sin\frac{ak_y}{2} - \sin ak_y \right], \quad (8)$$

$$f(\mathbf{k}) = e^{i\frac{ak_x}{\sqrt{3}}} + 2e^{-i\frac{ak_x}{2\sqrt{3}}} \cos\left(\frac{ak_y}{2}\right). \quad (9)$$

Note that near the two Dirac points $g_{\pm}(\mathbf{k}) = \pm 2\lambda_{\text{SOC}}$, and $\gamma_0 f(\mathbf{k}) = \hbar(iv_F k_x \mp v_F k_y)$, where $v_F = \sqrt{3}a\gamma_0/2\hbar$ is the Fermi velocity. Thus, one obtains a low-energy Hamiltonian which describes a quantum spin Hall insulator [11]. There is a topological phase transition to a band insulator as $|E_z|$ increases and crosses the critical field $E_{\text{cr}} = 2\lambda_{\text{SO}}/\ell$ [16].

The spin $s_z = \pm 1$ is a good quantum number. For the issue considered, there are no spin-flip transitions, and the spin index s_z can be considered a parameter in Hamiltonian (7). Otherwise, one can formally introduce bispinors and provide the orthogonality of eigenstates for different spins. Thus, there are four bands in the energy spectrum of the Hamiltonian (7). The eigenstates of the Hamiltonian (7) are

$$\psi_{s_z, \lambda, \mathbf{k}}(\mathbf{r}) = \frac{1}{\sqrt{\mathcal{A}}} |s_z, \lambda, \mathbf{k}\rangle e^{i\mathbf{k}\mathbf{r}}, \quad (10)$$

with

$$|s_z, \lambda, \mathbf{k}\rangle = \frac{1}{\sqrt{2\mathcal{E}_{s_z, \lambda}(\mathbf{k})[\mathcal{E}_{s_z, \lambda}(\mathbf{k}) - \Delta_{s_z}(\mathbf{k})]}} \times \begin{bmatrix} -\gamma_0 f(\mathbf{k}) \\ \mathcal{E}_{s_z, \lambda}(\mathbf{k}) - \Delta_{s_z}(\mathbf{k}) \end{bmatrix}, \quad (11)$$

corresponding to energies

$$\mathcal{E}_{s_z, \lambda}(\mathbf{k}) = \lambda \sqrt{\Delta_{s_z}^2(\mathbf{k}) + \gamma_0^2 |f(\mathbf{k})|^2}. \quad (12)$$

Here the band index $\lambda = \pm 1$ [for conduction ($\lambda = 1$) and valence ($\lambda = -1$) bands], \mathcal{A} is the quantization area, and

$$\Delta_{s_z}(\mathbf{k}) = \frac{1}{2}s_z g(\mathbf{k}) - \frac{\ell}{2}E_z. \quad (13)$$

Thus, the band gap depends on \mathbf{k} , s_z , and E_z and is given by $2|\Delta_{s_z}(\mathbf{k})|$.

Let the 2D nanostructure interact with the plane's quasi-monochromatic electromagnetic radiation. We consider the interaction when the wave propagates in a direction perpendicular to the nanostructure (XY). In this case the effect of the wave's magnetic field is excluded since in the z direction we have strong binding of the electrons. Thus, this traveling wave becomes a homogeneous quasiperiodic electric field with carrier frequency ω_0 and a slowly varying envelope. In general we assume an elliptically polarized wave:

$$\mathbf{E}(t) = f(t)(\hat{\mathbf{x}}E_{0x} \cos \omega_0 t + \hat{\mathbf{y}}E_{0y} \sin \omega_0 t). \quad (14)$$

The wave envelope is described by the Gaussian function

$$f(t) = \exp[-2 \ln 2(t - 2\mathcal{T}_p)^2 / \mathcal{T}_p^2], \quad (15)$$

where \mathcal{T}_p characterizes the pulse duration full width at half maximum. The latter is taken to be ten wave cycles: $\mathcal{T}_p = 10T$, where $T = 2\pi/\omega_0$.

We will work in the second quantization formalism, expanding the fermionic field operators on the basis of states

given in (10), that is,

$$\hat{\Psi}(\mathbf{r}) = \sum_{s_z, \lambda, \mathbf{k}} \hat{e}_{s_z, \lambda, \mathbf{k}} \psi_{s_z, \lambda, \mathbf{k}}(\mathbf{r}), \quad (16)$$

where $\hat{e}_{s_z, \lambda, \mathbf{k}}$ ($\hat{e}_{s_z, \lambda, \mathbf{k}}^\dagger$) is the annihilation (creation) operator for an electron with momentum \mathbf{k} , band λ , and spin s_z . The light-matter interaction part is taken in the length gauge, which is given in terms of the gauge-independent field $\mathbf{E}(t)$:

$$\hat{H}_{\text{int}} = e \int d\mathbf{r} \hat{\Psi}^\dagger(\mathbf{r}) \mathbf{r} \mathbf{E}(t) \hat{\Psi}(\mathbf{r}), \quad (17)$$

where e is the elementary charge. Taking into account expansion (16), the total Hamiltonian can be represented as follows:

$$\hat{H} = \sum_{s_z, \lambda, \mathbf{k}} \mathcal{E}_{s_z, \lambda}(\mathbf{k}) \hat{e}_{s_z, \lambda, \mathbf{k}}^\dagger \hat{e}_{s_z, \lambda, \mathbf{k}} + \hat{H}_{\text{int}}, \quad (18)$$

where the interaction part is given as follows:

$$\begin{aligned} \hat{H}_{\text{int}} = & ie \sum_{s_z, \lambda, \mathbf{k}, \mathbf{k}'} \delta_{\mathbf{k}'\mathbf{k}} \partial_{\mathbf{k}'} \mathbf{E}(t) \hat{e}_{s_z, \lambda, \mathbf{k}}^+ \hat{e}_{s_z, \lambda, \mathbf{k}'} \\ & + e \sum_{s_z, \lambda, \mathbf{k}} \mathbf{E}(t) \mathbf{D}_m(s_z, \lambda, \mathbf{k}) \hat{e}_{s_z, \lambda, \mathbf{k}}^+ \hat{e}_{s_z, \lambda, \mathbf{k}} \\ & + e \sum_{s_z, \lambda, \mathbf{k}} \mathbf{E}(t) \mathbf{D}_{\text{tr}}(s_z, \lambda, \mathbf{k}) \hat{e}_{s_z, \lambda, \mathbf{k}}^+ \hat{e}_{s_z, -\lambda, \mathbf{k}}. \end{aligned} \quad (19)$$

Here

$$\mathbf{D}_{\text{tr}}(s_z, \lambda, \mathbf{k}) = \langle s_z, \lambda, \mathbf{k} | i\partial_{\mathbf{k}} | s_z, -\lambda, \mathbf{k} \rangle \quad (20)$$

is the transition dipole moment (when multiplied by the electron charge) and

$$\mathbf{D}_m(s_z, \lambda, \mathbf{k}) = \langle s_z, \lambda, \mathbf{k} | i\partial_{\mathbf{k}} | s_z, \lambda, \mathbf{k} \rangle \quad (21)$$

is the Berry connection or mean dipole moment. These three terms in the light-matter interaction part provide the proper inclusion of inter- and intraband transitions [27,31]. The expressions for the transition dipole moment and Berry connection can be calculated using the spinor part of the wave function (11) and are given in the Appendix.

In order to develop a microscopic theory of the multiphoton interaction of a nanostructure with a strong radiation field we need to solve the master equation for the density matrix,

$$\rho_{\alpha, \beta}(s_z, \mathbf{k}, t) = \langle \hat{e}_{s_z, \beta, \mathbf{k}}^+(t) \hat{e}_{s_z, \alpha, \mathbf{k}}(t) \rangle, \quad (22)$$

where $\hat{e}_{s_z, \alpha, \mathbf{k}}(t)$ obeys the Heisenberg equation

$$i\hbar \frac{\partial \hat{e}_{s_z, \alpha, \mathbf{k}}(t)}{\partial t} = [\hat{e}_{s_z, \alpha, \mathbf{k}}(t), \hat{H}]. \quad (23)$$

Note that, due to the homogeneity of the problem, we need only the \mathbf{k} -diagonal elements of the density matrix. Taking into account Eqs. (22) and (23), the evolutionary equation

will be

$$\begin{aligned} i\hbar \frac{\partial \rho_{\alpha,\beta}(s_z, \mathbf{k}, t)}{\partial t} - ie\mathbf{E}(t) \frac{\partial \rho_{\alpha,\beta}(s_z, \mathbf{k}, t)}{\partial \mathbf{k}} &= [\mathcal{E}_{s_z,\alpha}(\mathbf{k}) - \mathcal{E}_{s_z,\beta}(\mathbf{k})] \rho_{\alpha,\beta}(s_z, \mathbf{k}, t) \\ &+ e\mathbf{E}(t) [\mathbf{D}_m(s_z, \alpha, \mathbf{k}) - \mathbf{D}_m(s_z, \beta, \mathbf{k})] \rho_{\alpha,\beta}(s_z, \mathbf{k}, t) \\ &+ e\mathbf{E}(t) [\mathbf{D}_{tr}(s_z, \alpha, \mathbf{k}) \rho_{-\alpha,\beta}(s_z, \mathbf{k}, t) - \mathbf{D}_{tr}(s_z, -\beta, \mathbf{k}) \rho_{\alpha,-\beta}(s_z, \mathbf{k}, t)]. \end{aligned} \quad (24)$$

The diagonal elements represent particle distribution functions for conduction bands, $N_c(s_z, \mathbf{k}, t) = \rho_{1,1}(s_z, \mathbf{k}, t)$, and for valence bands, $N_v(s_z, \mathbf{k}, t) = \rho_{-1,-1}(s_z, \mathbf{k}, t)$, and interband polarization $\rho_{1,-1}(s_z, \mathbf{k}, t) = P(s_z, \mathbf{k}, t)$. We just need equations for these quantities. We will also incorporate decay processes only into the equation for interband polarization by the damping term since homogeneous relaxation processes associated with each band population relaxing back to the initial distributions are on the picosecond timescale [43] and slow compared with the inhomogeneous one, which is expected to be in the 10–100 fs timescale as in graphene [44]. Thus, we have

$$i\hbar \frac{\partial N_c(s_z, \mathbf{k}, t)}{\partial t} - ie\mathbf{E}(t) \frac{\partial N_c(s_z, \mathbf{k}, t)}{\partial \mathbf{k}} = e[\mathbf{E}(t)\mathbf{D}_{tr}(s_z, c, \mathbf{k})P^*(s_z, \mathbf{k}, t) - \mathbf{E}(t)\mathbf{D}_{tr}^*(s_z, c, \mathbf{k})P(s_z, \mathbf{k}, t)], \quad (25)$$

$$i\hbar \frac{\partial N_v(s_z, \mathbf{k}, t)}{\partial t} - ie\mathbf{E}(t) \frac{\partial N_v(s_z, \mathbf{k}, t)}{\partial \mathbf{k}} = -e[\mathbf{E}(t)\mathbf{D}_{tr}(s_z, c, \mathbf{k})P^*(s_z, \mathbf{k}, t) - \mathbf{E}(t)\mathbf{D}_{tr}^*(s_z, c, \mathbf{k})P(s_z, \mathbf{k}, t)], \quad (26)$$

$$\begin{aligned} i\hbar \frac{\partial P(s_z, \mathbf{k}, t)}{\partial t} - ie\mathbf{E}(t) \frac{\partial P(s_z, \mathbf{k}, t)}{\partial \mathbf{k}} &= \{2\mathcal{E}_{s_z,1}(\mathbf{k}) + e\mathbf{E}(t) [\mathbf{D}_m(s_z, 1, \mathbf{k}) - \mathbf{D}_m(s_z, -1, \mathbf{k})] - i\hbar\Gamma\} P(s_z, \mathbf{k}, t) \\ &+ e\mathbf{E}(t)\mathbf{D}_{tr}(s_z, c, \mathbf{k}) [N_v(s_z, \mathbf{k}, t) - N_c(s_z, \mathbf{k}, t)], \end{aligned} \quad (27)$$

where Γ is the relaxation rate.

The obtained equations are a closed set of differential equations which should be solved with the proper initial conditions. We will solve the set of Eqs. (25), (26), and (27) with the initial conditions

$$\begin{aligned} P(s_z, \mathbf{k}, 0) &= 0, \quad N_c(s_z, \mathbf{k}, 0) = \frac{1}{1 + e^{\mathcal{E}_{s_z,1}(\mathbf{k})/T}}, \quad N_v(s_z, \mathbf{k}, 0) \\ &= \frac{1}{1 + e^{-\mathcal{E}_{s_z,1}(\mathbf{k})/T}}, \end{aligned} \quad (28)$$

where T is the temperature in energy units.

The optical excitation via a coherent radiation pulse induces transitions in the Fermi-Dirac sea which results in the surface current. The latter can be calculated by the following formula:

$$\mathbf{j}(t) = -e \sum_{s_z, \mathbf{k}, \lambda, \lambda'} \rho_{\lambda, \lambda'}(s_z, \mathbf{k}, t) \langle s_z, \lambda', \mathbf{k} | \widehat{\mathbf{V}}_{s_z}(\mathbf{k}) | s_z, \lambda, \mathbf{k} \rangle. \quad (29)$$

Here

$$\widehat{\mathbf{V}}_{s_z}(\mathbf{k}) = \hbar^{-1} \partial_{\mathbf{k}} \widehat{H} = \hbar^{-1} \begin{bmatrix} \frac{1}{2} s_z \partial_{\mathbf{k}} g(\mathbf{k}) & -\gamma_0 \partial_{\mathbf{k}} f(\mathbf{k}) \\ -\gamma_0 \partial_{\mathbf{k}} f^*(\mathbf{k}) & -\frac{1}{2} s_z \partial_{\mathbf{k}} g(\mathbf{k}) \end{bmatrix} \quad (30)$$

is the velocity operator. The surface current can be represented as follows:

$$\begin{aligned} \mathbf{j}(t) &= -e \sum_{s_z, \mathbf{k}, \lambda} \rho_{\lambda, \lambda}(s_z, \mathbf{k}, t) \langle s_z, \lambda, \mathbf{k} | \widehat{\mathbf{V}}_{s_z}(\mathbf{k}) | s_z, \lambda, \mathbf{k} \rangle \\ &- e \sum_{s_z, \mathbf{k}, \lambda} \rho_{-\lambda, \lambda}(s_z, \mathbf{k}, t) \langle s_z, \lambda, \mathbf{k} | \widehat{\mathbf{V}}_{s_z}(\mathbf{k}) | s_z, -\lambda, \mathbf{k} \rangle. \end{aligned} \quad (31)$$

The diagonal part can be written as

$$\langle s_z, \lambda, \mathbf{k} | \widehat{\mathbf{V}}_{s_z}(\mathbf{k}) | s_z, \lambda, \mathbf{k} \rangle = \partial_{\mathbf{k}} \mathcal{E}_{s_z, \lambda}(\mathbf{k}), \quad (32)$$

and the nondiagonal part can be calculated via transition dipole moments,

$$\langle s_z, \lambda, \mathbf{k} | \widehat{\mathbf{V}}_{s_z}(\mathbf{k}) | s_z, -\lambda, \mathbf{k} \rangle = \frac{2i}{\hbar} \mathcal{E}_{s_z, \lambda}(\mathbf{k}) \mathbf{D}_{tr}(s_z, \lambda, \mathbf{k}). \quad (33)$$

Taking into account Eqs. (32), (33), and the relation $\mathcal{E}_{s_z, -1}(\mathbf{k}) = -\mathcal{E}_{s_z, 1}(\mathbf{k})$, the surface current (31) can be written via distribution functions and interband polarization:

$$\begin{aligned} \mathbf{j}(t) &= -\frac{e}{\hbar} \frac{1}{(2\pi)^2} \sum_{s_z} \int_{BZ} d\mathbf{k} \{ \partial_{\mathbf{k}} \mathcal{E}_{s_z, 1}(\mathbf{k}) [N_c(s_z, \mathbf{k}, t) \\ &- N_v(s_z, \mathbf{k}, t)] + 2i\mathcal{E}_{s_z, 1}(\mathbf{k}) [\mathbf{D}_{tr}(s_z, 1, \mathbf{k}) P^*(s_z, \mathbf{k}, t) \\ &- \mathbf{D}_{tr}^*(s_z, 1, \mathbf{k}) P(s_z, \mathbf{k}, t)] \}. \end{aligned} \quad (34)$$

As is seen from Eq. (34), the surface current provides two sources for the generation of harmonic radiation. The first term is the intraband current. Under the action of the pump field, electrons are excited to the conduction band, leaving holes in the valence band. Then, the electron-hole pairs are accelerated by the field (14). This is evident when one makes a change in the variables and transforms the partial differential equations (25), (26), and (27) into ordinary ones. The new variables are t and $\mathbf{k} = \mathbf{k} - \mathbf{k}_E$, where

$$\mathbf{k}_E(t) = -\frac{e}{\hbar} \int_0^t \mathbf{E}(t') dt' \quad (35)$$

is the classical momentum given by the wave field. One should also make this transformation in the surface current (34). Intraband high harmonics are generated as a result of the independent motion of carriers in their respective bands. The second term in Eq. (34), which is defined via polarization, describes the interband current. Interband high harmonics are generated as a result of pump-field-induced recombination of

accelerated electron-hole pairs. Note that the relative contribution of intraband and interband high harmonics strongly depends on material and pump field parameters. In particular, when the energy gap is small compared with the driving wave frequency, the contributions of both mechanisms are essential.

III. GENERATION OF HIGH HARMONICS

We further examine the nonlinear response of a buckled hexagonal nanostructure considering the generation of harmonics at the multiphoton excitation. The wave-particle interaction will be characterized by the dimensionless parameters χ_{0x} , χ_{0y} , and χ_0 :

$$\chi_{0x,y} = \frac{eE_{0x,y}a}{\hbar\omega_0}, \quad \chi_0 = \sqrt{\chi_{0x}^2 + \chi_{0y}^2},$$

which represent the work of the wave electric field $E_{0x,y}$ on a lattice spacing in units of photon energy $\hbar\omega$. The average intensity of the pump wave expressed by χ_{0x} and χ_{0y} can be estimated as

$$I_0 = \chi_0^2 \times [\hbar\omega_0/\text{eV}]^2 \times [A/a]^2 \times 1.33 \times 10^{13} \text{ W cm}^{-2}. \quad (36)$$

Nonlinear effects take place when χ_0 becomes comparable to or larger than 1. In the scope of the two-band model we will consider moderately strong pump waves $\chi_0 \sim 1$ since at $\chi_0 \gg 1$ one should definitely take into account higher bands. For the photon energy we take $\hbar\omega_0 = 0.3 \text{ eV}$, and the intensity is taken to be 10^{11} W/cm^2 . The pulse duration will be $\mathcal{T}_p = 10\mathcal{T} = 138 \text{ fs}$. For the relaxation rate, we take $\Gamma = 0.5\mathcal{T}^{-1}$. For calculations, we assume room temperature.

The integration of Eqs. (25), (26), and (27) after the transformation from (t, \mathbf{k}) to $(t, \mathbf{k} - \mathbf{k}_E)$ is performed on the full reciprocal lattice unit cell with a grid of 10^4 points. The time integration is performed with the standard fourth-order Runge-Kutta algorithm. Thus, having solutions of Eqs. (25), (26), and (27) and then making an integration in equation (34), one can calculate the harmonic radiation spectrum with the help of a Fourier transform $\mathbf{j}(\omega)$ of the function $\mathbf{j}(t)$. Note that for a sufficiently large 2D sample the generated field will be

$$\mathbf{E}^{(g)}(t) = -\frac{4\pi}{c} \mathbf{j}(t). \quad (37)$$

Hence, we will characterize the emission strength of the s th harmonic by the dimensionless parameters

$$\eta_{x,y}(s) = \frac{4\pi}{c} \frac{|j_{x,y}(s\omega_0)|}{\sqrt{E_{0x}^2 + E_{0y}^2}}. \quad (38)$$

The typical nonlinear excitation of the Fermi sea is shown in Fig. 2 for silicene ($a = 3.86 \times 10^{-8} \text{ cm}$, $\gamma_0 = 1.087 \text{ eV}$, and $\lambda_{\text{SOC}} = 3.95 \text{ meV}$) and germanene ($a = 4.02 \times 10^{-8} \text{ cm}$, $\gamma_0 = 0.864 \text{ eV}$, and $\lambda_{\text{SOC}} = 46.5 \text{ meV}$). The particle distribution function $\mathcal{N}(\mathbf{k}, t_f)$ (in arbitrary units) after the interaction $t_f = 40\mathcal{T}$ is plotted. In Figs. 2(a) and 2(c) the wave is assumed to be polarized along the y axis, that is, along the $K_- - \Gamma - K_+$ direction in reciprocal space. Thus, the electric field is perpendicular to the mirror plane of the considered nanostructures. In Figs. 2(b) and 2(d) the wave is

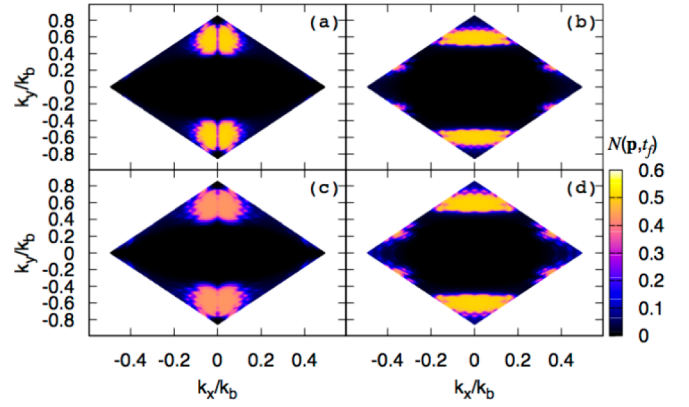


FIG. 2. Particle distribution function $N_c(\mathbf{k}, t_f)$ (in arbitrary units) after the interaction as a function of scaled dimensionless momentum components (k_x/k_b , k_y/k_b) for (a) and (b) silicene and (c) and (d) germanene. The wave is assumed to be linearly polarized with an intensity of 10^{11} W/cm^2 . In (a) and (c) the wave is assumed to be polarized along the y axis, while in (b) and (d) the wave is polarized along the x axis. Multiphoton excitation with the trigonal warping effect for the photon energy $\hbar\omega_0 = 0.3 \text{ eV}$ is shown.

polarized along the x axis (in the mirror plane). Multiphoton and strongly anisotropic excitation away from the Dirac points is clearly seen. In particular the excitation spots are prolonged along the wave polarization, which indicates that created particle-hole pairs are accelerated in the wave field. For the harmonic generation process, first, we consider the case when $E_z = 0$. The emission rates at high harmonics via the normalized field strength $\eta_y(s)$ for silicene, germanene, and stanene ($a = 4.7 \times 10^{-8} \text{ cm}$, $\gamma_0 = 0.784 \text{ eV}$, and $\lambda_{\text{SOC}} = 64.5 \text{ meV}$) are shown in Figs. 3 and 4. The wave is assumed to be linearly polarized along the y axis. The emission rate in the perpendicular direction is zero, $\eta_x(s) = 0$. High harmonics up to 13th order are obtained. In this case only odd harmonics are generated, reflecting the centrosymmetric nature preserved in the crystal lattices. To show the difference between crystals in

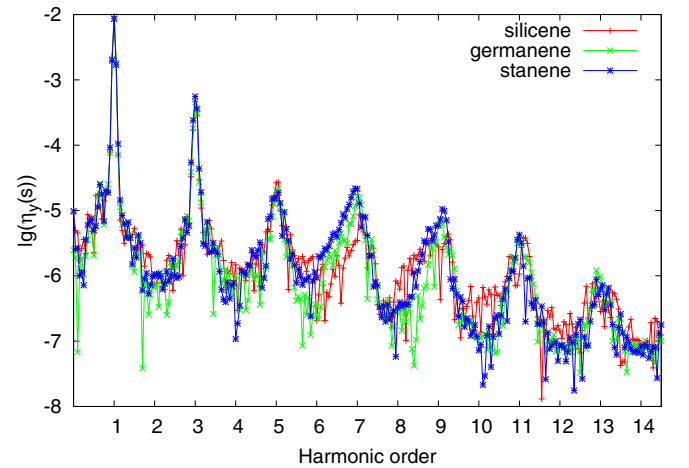


FIG. 3. The radiation spectrum via the logarithm of the normalized field strength $\eta_y(s)$ (in arbitrary units) for silicene, germanene, and stanene. The wave is assumed to be linearly polarized along the y axis, and $\chi_{0y} = 1.12$.

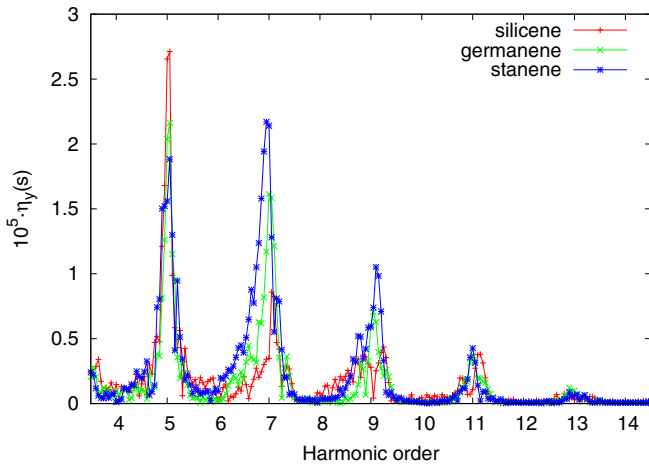


FIG. 4. The emission rate at high harmonics via the normalized field strength $\eta_y(s)$ for silicene ($\chi_{0y} = 1.12$), germanene ($\chi_{0y} = 1.16$), and stanene ($\chi_{0y} = 1.36$). The wave is assumed to be linearly polarized along the y axis. The emission rate in the perpendicular direction is zero, $\eta_x(s) = 0$.

Fig. 4 we plot only high harmonics in the basic scale. As can be seen, there is a qualitative difference for various crystals, and stanene shows more pronounced nonlinear properties. The emission rate at high harmonics for silicene for linearly polarized waves along the x and y axes is shown in Fig. 5. As can be seen, orienting the linearly polarized pump wave along these axes results in different harmonics spectra. The difference is essential for higher-order harmonics. This is because we have strongly anisotropic excitation away from the Dirac points (see Fig. 2).

The evolution of the high harmonic spectrum as a function of time is extracted from a windowed Fourier transform of the induced normalized field strength $\eta_y(t)$, where an $\exp(-10\pi x^4)$ window is scanned across 20 optical cycles. As is seen from Fig. 6, the emission of high harmonics takes place two times per wave cycle, corresponding to two maxima of the classical momentum $|\mathbf{k}_E(t)|$ given by the wave field (35). The

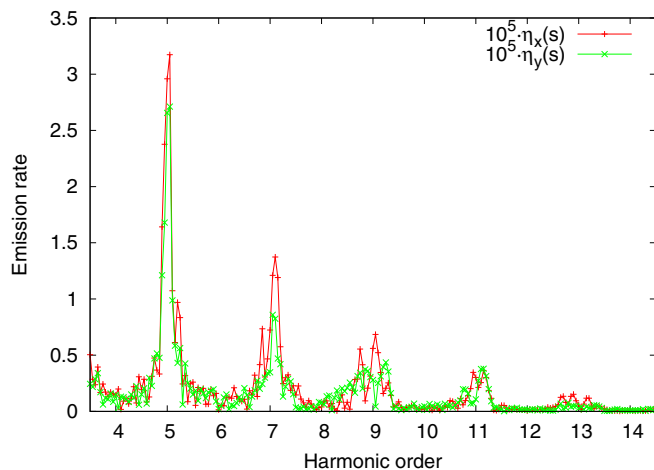


FIG. 5. The emission rate at high harmonics for silicene for linearly polarized waves along the x and y axes.

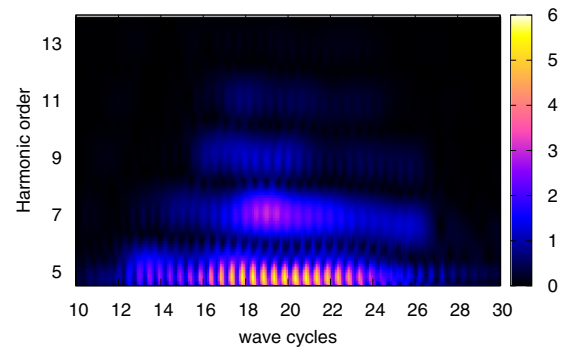


FIG. 6. The spectrogram of the high harmonic generation process via the windowed Fourier transform of the normalized field strength $\eta_y(t)$ for germanene. The wave is assumed to be linearly polarized along the y axis. The color bar represents the emission rate (arbitrary units) multiplied by 10^6 .

harmonic bursts are phase shifted from the pump wave. Thus, we have interplay between intra- and interband emission. For the taken parameters we have do not have a dominant interband mechanism compared with the one considered in Ref. [21].

Now we consider the case when $E_z \neq 0$. For the sublattice potential we take $\ell E_z = 0.2$ eV. In this case the topology of the bands is changed. In Fig. 7 the radiation spectra via the logarithm of the normalized field strengths $\eta_x(s)$ and $\eta_y(s)$ for germanene are shown in the x and y directions. The wave is assumed to be linearly polarized along the y axis. As is seen in the perpendicular to pump wave polarization direction, we have radiation of even harmonics. Note that this takes place only for the wave polarized along the $K_- - \Gamma - K_+$ direction.

The appearance of even harmonics strongly correlated to the topology of the bands. For the considered crystals the Berry curvature is nonzero (see the Appendix). However, at $E_z = 0$ when inversion symmetry is recovered by summing up on the spin index, the total Berry curvature becomes zero. For $E_z \neq 0$ the total Berry curvature is nonzero, which

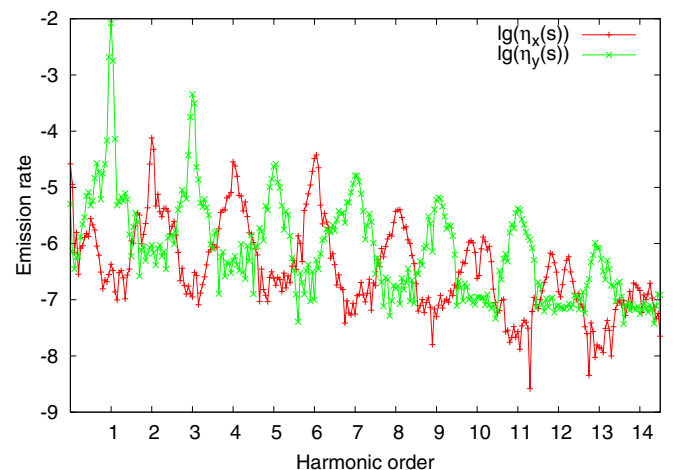


FIG. 7. The radiation spectrum via the logarithm of the normalized field strengths $\eta_x(s)$ and $\eta_y(s)$ for germanene at $\ell E_z = 0.2$ eV. The wave is assumed to be linearly polarized along the y axis.

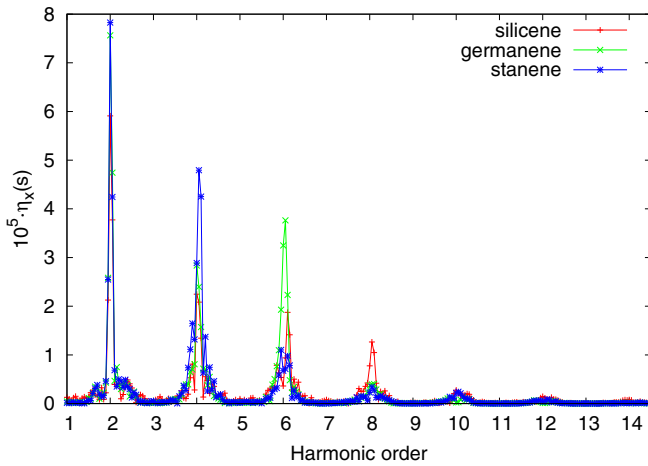


FIG. 8. The even-harmonic emission rate for the normalized field strength $\eta_x(s)$ for silicene, germanene, and stanene. The wave is assumed to be linearly polarized along the y axis.

is equivalent to an anomalous current which generates only even harmonics [40]. The even harmonics emission rates for silicene, germanene, and stanene are shown in Fig. 8. As can be seen, the germanene and stanene nanostructures show more pronounced nonlinear properties. Thus, the mechanism of generation of high harmonics in the considered nanostructures is different from the known atomic three-step model [41], and one can use this fact for the generation of high harmonics by a circularly polarized pump wave. In the atomic gas the HHG is impossible via a single circularly polarized laser pulse, and this is not conditioned by the global symmetry of the issue but the mechanism of HHG. So the novel graphenelike nanomaterials provide us with such an opportunity in the problem of HHG. To illustrate this in Figs. 9 and 10 we show the high harmonic radiation rates in germanene driven by a circularly polarized laser with the same intensity, and up to the 13th harmonic can be observed. As is seen for $E_z \neq 0$, even harmonics are also present. In both cases we have a selection

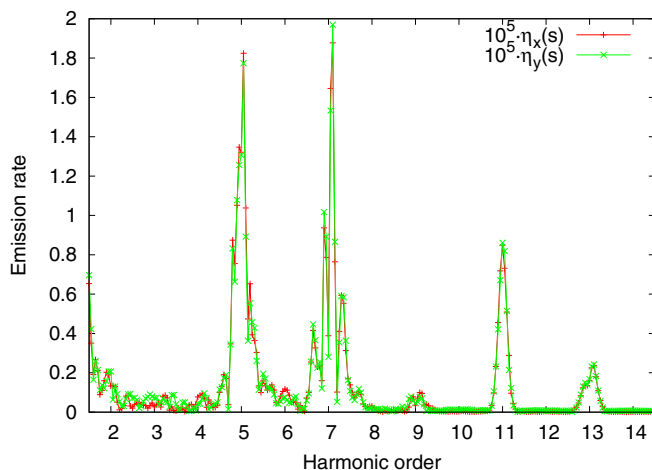


FIG. 9. The emission rate for harmonics polarized in both directions for germanene. The wave is assumed to be circularly polarized, and $E_z = 0$.

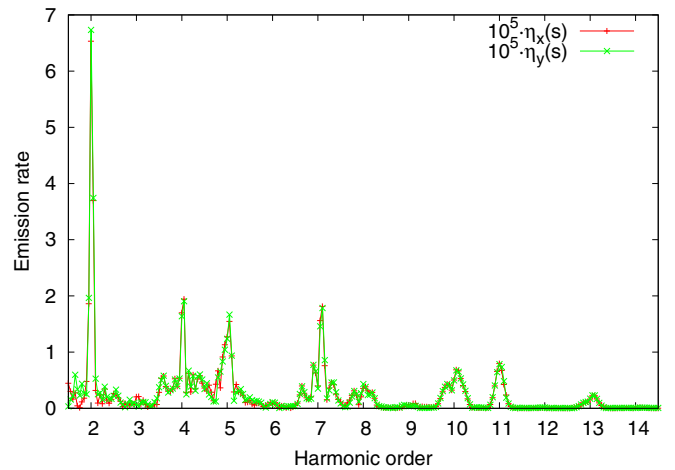


FIG. 10. The emission rate for harmonics polarized in both directions for germanene. The wave is assumed to be circularly polarized, and $\ell E_z = 0.2$ eV.

rule: every third harmonic is missing. This selection rule is a consequence of the threefold rotational symmetry of the considered crystals. In addition, as is seen from Figs. 9 and 10, the generated harmonics are almost circularly polarized. Thus, these materials can serve as an active medium of nanoscale size for the generation of circularly polarized even and odd high harmonics.

Let us estimate the intensity of the harmonics. For the perturbative regime, one can calculate the intensity of harmonics via high-order susceptibilities [45]. For the considered case, note that Eq. (37) at $L \gg \lambda$, where λ is the pump field wavelength and L is the characteristic size of the 2D sample, corresponds to the solution of Maxwell's wave equation with the given 2D source $\mathbf{j}(t)$ [34]. If we assume that the spectrum is measured at a fixed observation point in the forward (backward) propagation direction for the intensity of the s th harmonic, we will have $I_s = I_0 \sqrt{\eta_x^2 + \eta_y^2}/4$. For the setup of Figs. 3–10 with the chosen pump intensity $I_0 = 10^{11}$ W/cm² the average intensities of the harmonics are estimated to be $I_{2-11} \simeq 10^3$ – 1 W/cm². Note that this is the output from an atomically thin single-layer hexagonal nanostructure. It is clear that for the experimental realization one needs a multilayer 2D nanostructure [46]. We consider experimentally achievable values $N_L \sim 50$ monolayers [47] with a film thickness of ~ 20 nm. Since the film thickness is much smaller than the considered wavelengths, the harmonics' signals from all layers will be summed up constructively and enhanced by the N_L^2 factor.

IV. CONCLUSION

We have presented a nonlinear microscopic theory of a buckled hexagonal lattice interaction with strong electromagnetic radiation. The buckled hexagonal lattice system has been described by the four-band second-nearest-neighbor tight-binding model. The developed theory covers the full Brillouin zone of the hexagonal tight-binding nanostructure. For concreteness we have considered nonlinear excitation of

silicene, germanene, and stanene by midinfrared pump wave towards the high harmonic generation. The calculated spectra show high harmonics extending to the UV spectral region. It has also been shown that the role of the bands' topology in the nonlinear optical response of the buckled hexagonal lattice is quite considerable. In particular, when the total Berry curvature is nonzero, one can generate even harmonics perpendicularly polarized to the pump wave polarization direction. In addition, it has been shown that in the considered systems one can reach the efficient generation of circularly polarized high harmonics with a single circularly polarized pump wave of moderate intensity.

ACKNOWLEDGMENTS

This work was supported by the RA MES Science Committee in the frames of Research Project No. 18T-1C259.

APPENDIX: DIPOLE AND VELOCITY MATRIX ELEMENTS

The transition dipole matrix elements $\mathbf{D}_{\text{tr}}(s_z, \lambda, \mathbf{k})$ and Berry connections $\mathbf{D}_{\text{m}}(s_z, \lambda, \mathbf{k})$, used in the main text, are obtained by direct calculation with the help of Eqs. (11), (20), and (21). The transition dipole moments are explicitly given by

$$\text{Re } D_{\text{tr}}^{(x)}(s_z, 1, \mathbf{k}) = -\frac{a\gamma_0}{2\sqrt{3}\mathcal{E}_{s_z,1}(\mathbf{k})|f(\mathbf{k})|} \left[\cos\left(\frac{\sqrt{3}}{2}ak_x\right) \cos\left(\frac{ak_y}{2}\right) - \cos(ak_y) \right], \quad (\text{A1})$$

$$\text{Re } D_{\text{tr}}^{(y)}(s_z, 1, \mathbf{k}) = -\frac{a\gamma_0}{2\mathcal{E}_{s_z,1}(\mathbf{k})|f(\mathbf{k})|} \sin\left(\frac{\sqrt{3}}{2}ak_x\right) \sin\left(\frac{ak_y}{2}\right),$$

$$\begin{aligned} \text{Im } D_{\text{tr}}^{(x)}(s_z, 1, \mathbf{k}) &= -\frac{\sqrt{3}a\gamma_0\Delta_{s_z}(\mathbf{k})}{2\mathcal{E}_{s_z,1}^2(\mathbf{k})|f(\mathbf{k})|} \sin\left(\frac{\sqrt{3}}{2}ak_x\right) \cos\left(\frac{ak_y}{2}\right) \\ &+ \frac{\gamma_0a|f(\mathbf{k})|\lambda_{\text{SOC}}}{3\mathcal{E}_{s_z,1}^2(\mathbf{k})} s_z \sin\left(\frac{\sqrt{3}}{2}ak_x\right) \sin\left(\frac{ak_y}{2}\right), \end{aligned} \quad (\text{A2})$$

$$\text{Im } D_{\text{tr}}^{(y)}(s_z, 1, \mathbf{k}) = -\frac{a\gamma_0\Delta_{s_z}(\mathbf{k})}{2\mathcal{E}_{s_z,1}^2(\mathbf{k})|f(\mathbf{k})|} \left[\cos\left(\frac{\sqrt{3}}{2}ak_x\right) \sin\left(\frac{ak_y}{2}\right) + \sin(ak_y) \right] \quad (\text{A3})$$

$$-\frac{\gamma_0a|f(\mathbf{k})|s_z\lambda_{\text{SOC}}}{3\sqrt{3}\mathcal{E}_{s_z,1}^2(\mathbf{k})} \left[\cos\left(\frac{\sqrt{3}}{2}ak_x\right) \cos\frac{ak_y}{2} - \cos ak_y \right], \quad (\text{A4})$$

$$\mathbf{D}_{\text{tr}}(s_z, -1, \mathbf{k}) = \mathbf{D}_{\text{tr}}^*(s_z, 1, \mathbf{k}). \quad (\text{A5})$$

The Berry connection is a real quantity and is given by

$$D_{\text{m}}^{(x)}(s_z, \lambda, \mathbf{k}) = -\frac{a}{2|f(\mathbf{k})|^2\sqrt{3}} \left[\cos\left(\frac{\sqrt{3}}{2}ak_x\right) \cos\left(\frac{ak_y}{2}\right) - \cos(ak_y) \right] \left(1 + \frac{\Delta_{s_z}(\mathbf{k})}{\mathcal{E}_{s_z,\lambda}(\mathbf{k})} \right), \quad (\text{A6})$$

$$D_{\text{m}}^{(y)}(s_z, \lambda, \mathbf{k}) = -\frac{a}{2|f(\mathbf{k})|^2} \sin\left(\frac{\sqrt{3}}{2}ak_x\right) \sin\left(\frac{ak_y}{2}\right) \left(1 + \frac{\Delta_{s_z}(\mathbf{k})}{\mathcal{E}_{s_z,\lambda}(\mathbf{k})} \right). \quad (\text{A7})$$

In the equation of motion for the density matrix we need the difference $\Delta\mathbf{D}_{\text{m}}(s_z, \mathbf{k}) = \mathbf{D}_{\text{m}}(s_z, 1, \mathbf{k}) - \mathbf{D}_{\text{m}}(s_z, -1, \mathbf{k})$:

$$\Delta D_{\text{m}}^{(x)}(s_z, \mathbf{k}) = -\frac{\Delta_{s_z}(\mathbf{k})a}{\mathcal{E}_{s_z,1}(\mathbf{k})|f(\mathbf{k})|^2\sqrt{3}} \left[\cos\left(\frac{\sqrt{3}}{2}ak_x\right) \cos\left(\frac{ak_y}{2}\right) - \cos(ak_y) \right], \quad (\text{A8})$$

$$\Delta D_{\text{m}}^{(y)}(s_z, \mathbf{k}) = -\frac{\Delta_{s_z}(\mathbf{k})a}{\mathcal{E}_{s_z,1}(\mathbf{k})|f(\mathbf{k})|^2} \sin\left(\frac{\sqrt{3}}{2}ak_x\right) \sin\left(\frac{ak_y}{2}\right). \quad (\text{A9})$$

As is seen from Eqs. (A8) and (A9) at $\Delta_{s_z}(\mathbf{k}) = 0$ we have vanishing $\Delta\mathbf{D}_{\text{m}}(s_z, \mathbf{k})$. With the help of the Berry connection one can also calculate the Berry curvature,

$$\mathbf{B}_{\lambda}(s_z, \mathbf{k}) = \partial\mathbf{k} \times \mathbf{D}_{\text{m}}(s_z, \lambda, \mathbf{k}), \quad (\text{A10})$$

which is given by

$$B_{\lambda}^{(z)}(s_z, \mathbf{k}) = \frac{a^2 \gamma^2 \Delta_{s_z}(\mathbf{k})}{4\sqrt{3} \mathcal{E}_{s_z, \lambda}^3(\mathbf{k})} \left[2 \cos\left(\frac{\sqrt{3}}{2} ak_x\right) \sin\left(\frac{ak_y}{2}\right) - \sin(ak_y) \right] \\ + \frac{a^2 \gamma^2}{\mathcal{E}_{s_z, \lambda}^3(\mathbf{k})} \frac{s_z \lambda_{\text{SOC}}}{9} \left\{ \left[\cos\left(\frac{\sqrt{3}}{2} ak_x\right) \cos\left(\frac{ak_y}{2}\right) - \cos(ak_y) \right]^2 + 3 \sin^2\left(\frac{\sqrt{3}}{2} ak_x\right) \sin^2\left(\frac{ak_y}{2}\right) \right\}. \quad (\text{A11})$$

As is seen from Eq. (A11) $\mathbf{B}_1(s_z, \mathbf{k}) + \mathbf{B}_{-1}(s_z, \mathbf{k}) = 0$, in accordance with the definition [17]; at $\lambda_{\text{SOC}} = 0$ when inversion symmetry is broken, $\mathbf{B}_{\lambda}(s_z, \mathbf{k}) = -\mathbf{B}_{\lambda}(s_z, -\mathbf{k})$, and at $E_z = 0$, when inversion symmetry is recovered, summing up on the spin index, the total Berry curvature becomes zero: $\mathbf{B}_{\lambda}(1, \mathbf{k}) + \mathbf{B}_{\lambda}(-1, \mathbf{k}) = 0$.

The velocity is given by

$$V^{(x)}(s_z, \mathbf{k}) = \hbar^{-1} \partial_{k_x} \mathcal{E}_{s_z, 1}(\mathbf{k}) = -\frac{a\gamma_0^2 \sqrt{3}}{\hbar \mathcal{E}_{s_z, 1}(\mathbf{k})} \sin\left(\frac{\sqrt{3}}{2} ak_x\right) \cos\left(\frac{ak_y}{2}\right) - \frac{2as_z \Delta_{s_z}(\mathbf{k}) \lambda_{\text{SOC}}}{3\hbar \mathcal{E}_{s_z, 1}(\mathbf{k})} \sin\left(\frac{\sqrt{3}}{2} ak_x\right) \sin\left(\frac{ak_y}{2}\right), \quad (\text{A12})$$

$$V^{(y)}(s_z, \mathbf{k}) = \hbar^{-1} \partial_{k_y} \mathcal{E}_{s_z, 1}(\mathbf{k}) = -\frac{a\gamma_0^2}{\hbar \mathcal{E}_{s_z, 1}(\mathbf{k})} \left[\cos\left(\frac{\sqrt{3}}{2} ak_x\right) \sin\left(\frac{ak_y}{2}\right) + \sin(ak_y) \right] \\ + \frac{2as_z \Delta_{s_z}(\mathbf{k}) \lambda_{\text{SOC}}}{3\sqrt{3} \hbar \mathcal{E}_{s_z, 1}(\mathbf{k})} \left[\cos\left(\frac{\sqrt{3}}{2} ak_x\right) \cos\left(\frac{ak_y}{2}\right) - \cos(ak_y) \right]. \quad (\text{A13})$$

-
- [1] K. S. Novoselov, A. K. Geim, S. V. Morozov, D. Jiang, Y. Zhang, S. V. Dubonos, I. V. Grigorieva, and A. A. Firsov, *Science* **306**, 666 (2004).
- [2] A. H. Castro Neto, F. Guinea, N. M. R. Peres, K. S. Novoselov, and A. K. Geim, *Rev. Mod. Phys.* **81**, 109 (2009).
- [3] B. Lalmi, H. Oughaddou, H. Enriquez, A. Kara, S. Vizzini, B. Ealet, and B. Aufray, *Appl. Phys. Lett.* **97**, 223109 (2010).
- [4] P. Vogt, P. De Padova, C. Quaresima, J. Avila, E. Frantzeskakis, M. C. Asensio, A. Resta, B. Ealet and G. Le Lay, *Phys. Rev. Lett.* **108**, 155501 (2012).
- [5] A. Fleurence, R. Friedlein, T. Ozaki, H. Kawai, Y. Wang, and Y. Yamada-Takamura, *Phys. Rev. Lett.* **108**, 245501 (2012).
- [6] E. Bianco, S. Butler, S. Jiang, O. D. Restrepo, W. Windl, and J. E. Goldberger, *Acs Nano* **7**, 4414 (2013).
- [7] M. E. Davila, L. Xian, S. Cahangirov, A. Rubio, and G. L. Lay, *New J. Phys.* **16**, 095002 (2014).
- [8] F. F. Zhu, W. J. Chen, Y. Xu, C. L. Gao, D. D. Guan, C. H. Liu, D. Qian, S. C. Zhang, and J. F. Jia, *Nat. Mater.* **14**, 1020 (2015).
- [9] N. D. Drummond, V. Zolyomi, and V. I. Falko, *Phys. Rev. B* **85**, 075423 (2012).
- [10] C. C. Liu, H. Jiang, and Y. Yao, *Phys. Rev. B* **84**, 195430 (2011).
- [11] C. C. Liu, W. Feng, and Y. Yao, *Phys. Rev. Lett.* **107**, 076802 (2011).
- [12] M. Ezawa, *New J. Phys.* **14**, 033003 (2012).
- [13] M. Ezawa, *Phys. Rev. Lett.* **109**, 055502 (2012).
- [14] M. Ezawa, *Phys. Rev. B* **86**, 161407(R) (2012).
- [15] M. Ezawa, *Phys. Rev. Lett.* **110**, 026603 (2013).
- [16] M. Ezawa, *J. Phys. Soc. Jpn.* **84**, 121003 (2015).
- [17] D. Xiao, M. C. Chang, and Q. Niu, *Rev. Mod. Phys.* **82**, 1959 (2010).
- [18] S. Ghimire, A. D. DiChiara, E. Sistrunk, P. Agostini, L. F. DiMauro, and D. A. Reis, *Nat. Phys.* **7**, 138 (2011).
- [19] O. Schubert, M. Hohenleutner, F. Langer, B. Urbanek, C. Lange, U. Huttner, D. Golde, T. Meier, M. Kira, S. W. Koch, and R. Huber, *Nat. Photonics* **8**, 119 (2014).
- [20] G. Vampa, T. J. Hammond, N. Thire, B. E. Schmidt, F. Legare, C. R. McDonald, T. Brabec, and P. B. Corkum, *Nature (London)* **522**, 462 (2015).
- [21] G. Vampa, C. R. McDonald, G. Orlando, P. B. Corkum, and T. Brabec, *Phys. Rev. B* **91**, 064302 (2015).
- [22] G. Ndabashimiye, S. Ghimire, M. Wu, D. A. Browne, K. J. Schafer, M. B. Gaarde, and D. A. Reis, *Nature (London)* **534**, 520 (2016).
- [23] Y. S. You, D. A. Reis, and S. Ghimire, *Nat. Phys.* **13**, 345 (2017).
- [24] H. Liu, C. Guo, G. Vampa, J. L. Zhang, T. Sarmiento, M. Xiao, P. H. Bucksbaum, J. Vuckovic, S. Fan, and D. A. Reis, *Nat. Phys.* **14**, 1006 (2018).
- [25] S. A. Mikhailov, *Europhys. Lett.* **79**, 27002 (2007).
- [26] S. A. Mikhailov and K. Ziegler, *J. Phys.: Condens. Matter* **20**, 384204 (2008).
- [27] H. K. Avetissian, A. K. Avetissian, G. F. Mkrtchian, and Kh. V. Sedrakian, *Phys. Rev. B* **85**, 115443 (2012).
- [28] H. K. Avetissian, G. F. Mkrtchian, K. G. Batrakov, S. A. Maksimenko, and A. Hoffmann, *Phys. Rev. B* **88**, 165411 (2013).
- [29] P. Bownan, E. Martinez-Moreno, K. Reimann, T. Elsaesser, and M. Woerner, *Phys. Rev. B* **89**, 041408 (2014).
- [30] I. Al-Naib, J. E. Sipe, and M. M. Dignam, *Phys. Rev. B* **90**, 245423 (2014).
- [31] I. Al-Naib, J. E. Sipe, and M. M. Dignam, *New J. Phys.* **17**, 113018 (2015).
- [32] L. A. Chizhova, F. Libisch, and J. Burgdorfer, *Phys. Rev. B* **94**, 075412 (2016).

- [33] H. K. Avetissian and G. F. Mkrtchian, *Phys. Rev. B* **94**, 045419 (2016).
- [34] H. K. Avetissian, A. G. Ghazaryan, G. F. Mkrtchian, and Kh. V. Sedrakian, *J. Nanophotonics* **11**, 016004 (2017).
- [35] L. A. Chizhova, F. Libisch, and J. Burgdorfer, *Phys. Rev. B* **95**, 085436 (2017).
- [36] D. Dimitrovski, L. B. Madsen, and T. G. Pedersen, *Phys. Rev. B* **95**, 035405 (2017).
- [37] N. Yoshikawa, T. Tamaya, and K. Tanaka, *Science* **356**, 736 (2017).
- [38] H. K. Avetissian and G. F. Mkrtchian, *Phys. Rev. B* **97**, 115454 (2018).
- [39] G. Le Breton, A. Rubio, and N. Tancogne-Dejean, *Phys. Rev. B* **98**, 165308 (2018).
- [40] H. Liu, Y. Li, Y. S. You, S. Ghimire, T. F. Heinz, and D. A. Reis, *Nat. Phys.* **13**, 262 (2017).
- [41] M. Lewenstein, Ph. Balcou, M. Yu. Ivanov, A. L'Huillier, and P. B. Corkum, *Phys. Rev. A* **49**, 2117 (1994).
- [42] C. L. Kane and E. J. Mele, *Phys. Rev. Lett.* **95**, 226801 (2005).
- [43] X. S. Ye, Z. G. Shao, H. Zhao, L. Yang, and C. L. Wang, *RSC Adv.* **4**, 21216 (2014).
- [44] E. Malic, T. Winzer, E. Bobkin, and A. Knorr, *Phys. Rev. B* **84**, 205406 (2011).
- [45] A. V. Korovin, F. T. Vasko, and V. V. Mitin, *Phys. Rev. B* **62**, 8192 (2000).
- [46] H. S. Tsai, Y. Z. Chen, H. Medina, T. Y. Su, T. S. Chou, Y. H. Chen, Y. L. Chueh, and J. H. Liang, *Phys. Chem. Chem. Phys.* **17**, 21389 (2015).
- [47] A. L. Friedman, J. L. Tedesco, P. M. Campbell, J. C. Culbertson, E. Aifer, F. K. Perkins, R. L. Myers-Ward, J. K. Hite, C. R. Eddy, Jr., G. G. Jernigan, and D. K. Gaskill, *Nano Lett.* **10**, 3962 (2010).